PNAS RESEARCH ARTICLE | APPLIED PHYSICAL SCIENCES OPEN ACCESS

Rheology of debris flow materials is controlled by the distance from jamming

Robert Kostynick[a,b,1], Hadis Matinpour[c,1], Shravan Pradeep[b,1], Sarah Haber[d], Alban Sauret[c], Eckart Meiburg[c], Thomas Dunne[e], Paulo Arratia[f], and Douglas Jerolmack[b,f,2]

Edited by David Weitz, Harvard University, Cambridge, MA; received May 31, 2022; accepted September 18, 2022

Debris flows are dense and fast-moving complex suspensions of soil and water that threaten lives and infrastructure. Assessing the hazard potential of debris flows requires predicting yield and flow behavior. Reported measurements of rheology for debris flow slurries are highly variable and sometimes contradictory due to heterogeneity in particle composition and volume fraction (ϕ) and also inconsistent measurement methods. Here we examine the composition and flow behavior of source materials that formed the post-wildfire debris flows in Montecito, CA, in 2018, for a wide range of ϕ that encapsulates debris flow formation by overland flow. We find that shear viscosity and yield stress are controlled by the distance from jamming, $\Delta\phi = \phi_m - \phi$, where the jamming fraction ϕ_m is a material parameter that depends on grain size polydispersity and friction. By rescaling shear and viscous stresses to account for these effects, the data collapse onto a simple nondimensional flow curve indicative of a Bingham plastic (viscoplastic) fluid. Given the highly nonlinear dependence of rheology on $\Delta\phi$, our findings suggest that determining the jamming fraction for natural materials will significantly improve flow models for geophysical suspensions such as hyperconcentrated flows and debris flows.

jamming | soft matter | geomorphology | debris flow

Significance

Debris flows are fast-flowing and dangerous slurries of soil and water that often form when intense rainfall soaks hillsides burned by wildfire. As climate change intensifies this hazard, models capable of predicting failure and flow behaviors are needed. Here we capitalize on recent progress in the physics of dense suspensions, to determine how the physical and chemical composition of natural hillslope soils controls the viscosity and yield stress of debris flows. We show how a simple flow model—previously developed for idealized suspensions—can be extended to highly heterogeneous, natural debris flow materials. This model reconciles previously contradictory observations and could help to improve computer models that assess the hazard potential of debris flows in the field.

When intense rainfall soaks the soil on steep mountain hillsides, water and particulates can mix to form a dense, viscous suspension called a debris flow (1). Debris flows may form catastrophically, such as landslides that collapse into valley-bottom channels and mix with river water (2), or gradually, as overland flow on steep hillsides progressively entrains soil (3, 4). Debris flows are particularly hazardous due to their high speed and density (5) and because their fluidity allows them to spread rapidly when flows become unconfined—for example, upon exiting a canyon (6). As debris flows spread they slow down and eventually "freeze," implying that a minimum shear stress (τ) is necessary to sustain flow (7–9). A simple rheological model that captures the observed phenomenology is the widely applied Herschel–Bulkley equation,

$$\tau = \tau_o + k\dot{\gamma}^n, \quad [1]$$

where τ [Pa] is the shear stress, τ_o [Pa] is the yield stress, $\dot{\gamma}$ [s^{-1}] is the shear rate, and k is an empirical coefficient with dimension that depends on the value of the exponent. The exponent n is the flow index, where in general, $n < 1$ corresponds to shear thinning, and $n > 1$ is associated with shear thickening behavior.

In typical constant volume steady-shear rheology experiments, like those we present in this study, a suspension with fixed solid volume fraction ϕ is placed in a fluid gap of thickness h, and one boundary is sheared at a constant velocity u while the shear stress is measured. The resulting data are used to produce a flow curve, τ vs. $\dot{\gamma} \approx u/h$, from which the shear viscosity $\eta = \tau/\dot{\gamma}$ can be obtained. Due to its flexibility, the Herschel–Bulkley model has been applied widely to fit the flow curves of debris flow materials (10–14). Parameter values, however, are inconsistent among different studies and can show extreme sensitivity to ϕ and also to material composition (clay/silt/sand content) (8, 10, 15, 16). For example, τ_o increases rapidly with ϕ, but the functional form appears to vary among studies (8, 16, 17), and flow behavior of sand–water mixtures was found to change from highly shear thinning ($n < 0.5$) to Bingham-like ($n \approx 1$) with the addition of small amounts of clay (18). While most reported debris flow data indicate apparent shear thinning behavior ($n < 1$), some mixtures appear to exhibit shear thickening ($n > 1$) (9, 10, 12–14, 18–22). Thus, the Herschel–Bulkley model provides a compact description of the flow curve for a given sample, but model results may not be extrapolated to different settings or geometries because the physical meaning of the fitting parameters is unclear (23). More broadly, Eq. **1** is insufficient for describing natural debris flows because it does not include feedbacks among ϕ, $\dot{\gamma}$, and pore fluid pressure (24–26). In particular, simulations for debris flow failure and runout emphasize the importance of transient pore

Author contributions: A.S., E.M., T.D., P.A., and D.J. designed research; R.K., H.M., S.P., and S.H. performed research; D.J. supervised research; T.D. and D.J. performed field work; S.P. contributed new reagents/analytic tools; R.K., H.M., S.P., and S.H. analyzed data; and R.K., S.P., and D.J. wrote the paper.

The authors declare no competing interest.

This article is a PNAS Direct Submission.

[1]R.K., H.M., and S.P. contributed equally to this work.

[2]To whom correspondence may be addressed. Email: sediment@sas.upenn.edu.

This article contains supporting information online at https://www.pnas.org/lookup/suppl/doi:10.1073/pnas.2209109119/-/DCSupplemental.

Published October 24, 2022.

fluid pressure (27, 28). Nevertheless, these models still require constitutive relations among stress, shear rate, and volume fraction.

Physically Based Rheological Models. Since the pioneering experiments of Bagnold (29), much progress has been made in understanding the physical basis for rheology in idealized suspensions and granular flows. In the inertial flow regime where collisions are significant, Bagnold found that the shear stress scales like $\tau \sim \rho_p d^2\dot{\gamma}^2$, where ρ_p and d are particle density and diameter, respectively. Nondimensionalization of the stresses by the confining pressure, P^p, leads to the so-called "$\mu(I)$ rheology" that is often used to describe dense granular flows, wherein friction $\mu \equiv \tau/P^p$ is modeled as a monotonic function of the dimensionless shear rate $I \equiv d\dot{\gamma}\sqrt{\rho_p/P^p}$ (30–32). Note that the inertial number I can also be interpreted as the ratio of two timescales: a macrotimescale associated with strain around a particle, $t_{macro} = 1/\dot{\gamma}$, and a microtimescale associated with particle inertia, $t_{micro} = d\sqrt{\rho_p/P^p}$ (33). When grains are suspended in a viscous fluid like water, however, the viscous stress of the carrier fluid becomes relevant. It was found recently that viscous stress dominates over particle inertia when the Stokes number $St \equiv \rho_p d^2\dot{\gamma}/\eta_f < 10$, where η_f is the viscosity of the suspending fluid (34). The microtimescale in the viscous regime becomes $t_{micro} = \eta_f/P^p$, and the dimensionless shear rate becomes the viscous number $J \equiv \eta_f\dot{\gamma}/P^p$. The $\mu(J)$ rheology successfully describes viscous suspensions (33, 35) and sediment transport (36). For many common materials such as clay suspensions, however, there is an additional stress to be considered: the yield stress arising from interparticle attraction (cohesion), which is manifest as a residual internal stress in the quasistatic ($\dot{\gamma} \to 0$) limit. Cohesion acts as a kind of confining stress that tends to resist dilation during flow (37). In the framework of granular suspensions this suggests that the relevant t_{micro} for materials with significant yield stress (i.e., $\tau_o \gg P^p$) is instead a characteristic timescale of the material, $t_{micro} = \eta(\phi)/\tau_o$, as proposed by Coussot (17). Accordingly, the relevant dimensionless stress becomes $\tau^* \equiv \tau/\tau_o$, and the dimensionless shear rate is $\Gamma \equiv \eta(\phi)\dot{\gamma}/\tau_o$. Note that Γ is the inverse of the Bingham number, which characterizes the ratio of elastic and viscous stresses; however, here the viscous stress $\eta(\phi)\dot{\gamma}$ is associated with the effective viscosity of the suspension $\eta(\phi)$, not the carrier fluid (8, 17, 38). Coussot showed that the $\tau^*(\Gamma)$ rheology collapsed much of the variability in flow curves of clay suspensions (17)—a model mud system (8, 17, 38). To summarize, inertial, viscous, and cohesive (yield) stresses may each be associated with a distinct microtimescale for particle motion. Nondimensionalization of measured flow curves can be used to diagnose which stress may be dominant because each stress produces a different scaling behavior. More recent simulations (37) and experiments (34) indicate that these stresses are additive. For suspensions in which some or all of the stresses are significant, it appears that the inertial number may be generalized to account for all of them (34, 37).

An important concept introduced above is $\eta(\phi)$, which describes the functional dependence of suspension viscosity on the volume fraction of particles suspended. One way to think about the initiation and cessation of flows of dense suspensions is as a jamming transition (39)—that is, a continuous transition between rigid and flowing states where flow is arrested in the direction of applied shear at a jamming fraction $\phi = \phi_m$ (33, 35). The parameter ϕ_m for suspensions is analogous to the critical-state volume fraction in soil mechanics (40). In this framework, suspension viscosity is primarily controlled by the distance from jamming, $\Delta\phi = \phi_m - \phi$. As particles are added to a fluid, the effective viscosity increases, first from drag and hydrodynamic interactions among particles and eventually (as $\phi \to \phi_m$) due to geometric confinement and friction among the grains (35). A well-known result is that suspension viscosity diverges on approach to jamming as $\eta(\phi) \propto (\Delta\phi)^{-2}$ (41, 42). In this manner viscosity acts as an order parameter that describes how fluid-like the suspension is across the jamming transition; a similar concept has been proposed for granular flow rheology models using the concept of fluidity, which is an inverse viscosity parameter (43, 44). Boyer et al. (33) presented a model for granular suspensions that effectively captures the observed dependence of η on ϕ and also on the ϕ-dependent granular contact friction μ^c:

$$\eta(\phi)/\eta_f = 1 + \frac{5}{2}\cdot\phi\Big(1-\phi/\phi_m\Big)^{-1} + \mu^c(\phi)\Big(\phi/\Delta\phi\Big)^2. \quad [2]$$

The parameter ϕ_m depends on material properties: increased surface roughness decreases ϕ_m (45, 46), whereas increased grain size polydispersity increases ϕ_m by allowing higher packing densities (47). In the dilute regime ($\phi \ll \phi_m$), the third term in Eq. **2** that represents granular interactions is negligible. For dense suspensions corresponding to small $\Delta\phi$, however, the third term is dominant. For suspensions close to the jamming limit, changing ϕ or ϕ_m by even 1% can change the effective viscosity by orders of magnitude.

Summary of This Study. In this study we examine soil sampled from the source areas of the 2018 debris flows that occurred in the Santa Ynez Mountains in Montecito, CA (USA), a devastating event that resulted in 23 fatalities and 408 damaged homes (4). Previous field studies have constrained the timing, generation, runout, and damage associated with the debris flows (4, 5). A simulation study of the Montecito debris flows examined the sensitivity of existing numerical models to constitutive equations and the value of ϕ_m (28). The goals of this study are to test the applicability of the rheological models described above for capturing the flow behavior of suspensions of natural soils and to relate model parameters to the physical and chemical composition of particulates. We conduct an exhaustive laboratory examination of the steady-shear flow behavior of hillslope soils, when mixed with water over a wide range of ϕ values—from dilute to nearly jammed. We present experimental determination of three parameters: ϕ_m, μ^c, and τ_o. We find striking confirmation of Eq. **2** from these data, despite the wide heterogeneity in grain size and mineralogy of the natural soils. Moreover, we demonstrate that ϕ_m varies systematically with grain size polydispersity and friction. For dense slurries we find that yield stress is dominant and varies nonlinearly with the distance from jamming $\Delta\phi$, while the control of measured chemical composition is ambiguous. Our flow curve measurements are well described by the $\tau^*(\Gamma)$ rheology, and we find a compact constitutive equation that accounts for shear rate and volume fraction effects. These results clarify the distinct material controls on the rheology of debris flow slurries, reconcile disparate observations and models, and provide a protocol for practitioners to determine the relevant parameters in a straightforward manner.

Results

Field Estimates of Debris Flow Properties. In December of 2017, a large wildfire occurred on the steep hillslopes of the Santa Ynez mountains north of Montecito, California (USA). Vegetation was almost completely incinerated to soil depths of 3 to 5 cm; root mass and humic carbonaceous materials were removed. The average bulk density of this burned topsoil was 1,400 kg/m^3,

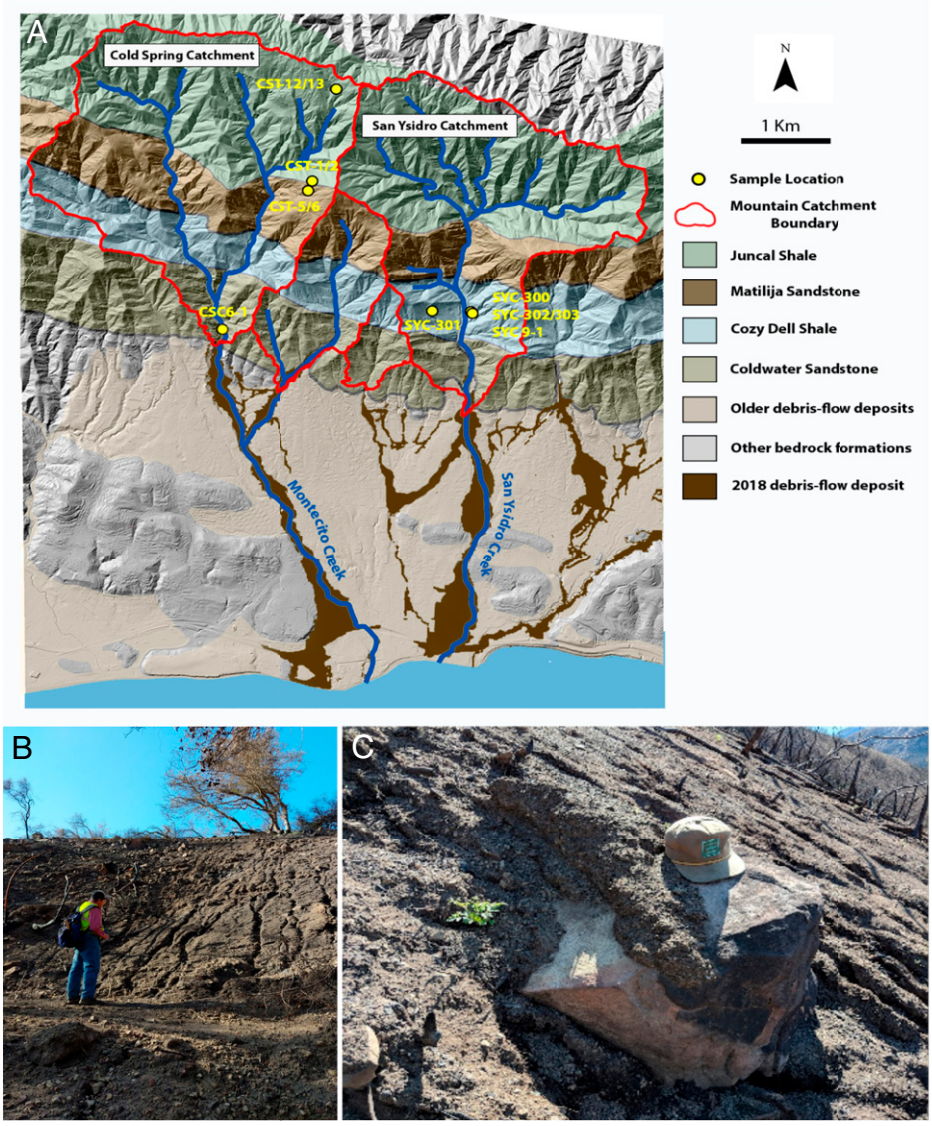

Fig. 1. Field setting. (*A*) Digital elevation model of the Montecito region. Sample names used throughout this study are shown in yellow. Main catchment regions are designated in red, with the two primary catchments and fluvial channels of interest labeled. Major lithological units are shown throughout and denoted in the legend. Debris flow deposits from the 2018 event are indicated as a dark brown lithological unit with primary flow paths following the channel paths. (*B*) Field image showing a site of source material used for rheologic testing. Rills are the concentrated zones of erosion on the hillslope. (*C*) Close up of hillslope soil deposited on a boulder, showing that source materials formed viscous, yield stress flows.

whereas the unburned subsoil retained its sparser roots and an average bulk density of 1,700 kg/m^3 (4). Assuming a grain density of 2,700 kg/m^3, this indicates that burned topsoil had an average soil volume fraction of $\phi = 0.52$, while unburned subsoil had an average value of $\phi = 0.63$. Three weeks later, intense rainfall over a 10 to 15 min period resulted in concentrated hillside erosion in the form of a dense network of rills (4). As rainwater flowed down slopes $>35^o$, it progressively entrained soil and increased ϕ to create fully formed debris flows—with yield stress features such as levees and lobes—over distances of ∼100 m (Fig. 1). Using rainfall–runoff modeling and lidar topography data, a recent study estimated an average volume fraction of $\phi = 0.51$ for debris flow slurries issuing from hillslope rills across the area (4). This same study indicated that burned surface soils maintained some degree of cohesion, inferring an effective cohesive stress on the order 10^2 Pa.

The hillslope-generated debris flows, containing particles ranging in size from clay (∼20 μm) to coarse sand (∼1 mm), accumulated in valley-bottom channels where they entrained boulders up to ∼6 m in diameter (5, 48). As the debris flows exited the canyons and progressed down fans, they spread outward from the channel leaving deposits (Fig. 1*A*). Although hillslope materials were generally coarser than debris flow deposits on the downstream fans, Kean et al. (5) found that the average gravel–sand–silt–clay fractions were similar. Thus, mechanical behavior inferred from the downstream flows and their deposits may help to constrain the nature of debris flows generated on hillslopes. The shear stress of debris flows observed downstream of the canyon outlets can be estimated as $\tau = \rho g H S$, while shear rate is roughly $\dot{\gamma} = u/H$, where $\rho = 2{,}000$ kg/m^3 is the assumed suspension density and g is gravity. Using representative values for flow depth $H = 2$ m, surface slope $S = 0.04$, and flow speed $u = 4$ m/s (5, 28), we estimate $\tau = 1{,}600$ Pa and $\dot{\gamma} = 2$ s^{-1}. We observed frozen deposits with depths of roughly 20 cm, from which we infer a yield stress of roughly $\tau_o = 200$ Pa. The flow viscosity can be estimated as $\eta = \tau/\dot{\gamma} = 800$ Pa · s. While these estimates are crude, τ_o of order 10^2 Pa and η of order 10^2 Pa · s are consistent with expectations for high-ϕ debris flows (10, 49–51).

The Reynolds number associated with these flows, $Re = \rho u H/\eta \sim 10^1$, indicates laminar conditions. Conservatively estimating the Stokes number—using a grain size representative of the coarsest hillslope material, $d = 1$ mm—indicates that flows remained in the viscous regime ($St < 10$), except for the boulder-rich fronts, which were certainly inertial.

Composition of Source Materials. Over the 2 mo following the event, we sampled burned topsoils (down to 5 cm depth) and unburned subsoils (5 to 20 cm depth) from interrill areas on hillslopes in two watersheds within the Santa Ynez mountains that served as source materials (*SI Appendix*, Table S1) for the debris flows (Fig. 1). Our sampling strategy was designed to examine potential controls of lithology, burning, and position within the watershed on the composition and rheology of soils (*SI Appendix*, Text S1). Despite significant variation among samples, however, we found no systematic change in soil composition due to any of these factors (*SI Appendix*, Table S2 and Fig. S1). The soils were sieved to remove particles >500 μm in order to prevent clogging of grains in the relatively small gap of the rheometer. Although removing larger grains may influence the mechanical properties of soil slurries, the volume fraction removed was <5% for all samples. Additional experiments on unsieved samples were run in a different rheometer and produced qualitatively similar results (*SI Appendix*, Fig. S2) but could not be interpreted quantitatively due to size segregation and sedimentation effects (see below).

Sonication was applied to aqueous suspensions of the soils in order to break up aggregates, and grain size was measured using a laser diffraction device (*Materials and Methods*). All soil samples contained particles ranging from clay to coarse sand, had a mean grain size in the very fine sand range (60 to 120 μm), and displayed significant peaks in the fine silt (20 to 30 μm) and fine sand (∼200 μm) ranges (Fig. 2 and *SI Appendix*, Table S2). The biggest difference among samples was the fraction of particles larger than fine sand (>250 μm; Fig. 2). For comparison to other studies, we approximate polydispersity by fitting a log-normal distribution to the data and computing m_3/m_2^2, where $m_k \equiv M_k/{M_1}^k$ and M_k is the kth moment of the distribution (52). Extrapolating results from simulations of idealized spheres (52, 53), we anticipate that the factor ∼3 range in polydispersity values may give rise to variation in the jamming fraction of roughly 10% among the samples; however, we know of no studies that have examined ϕ_m for suspensions with such large polydispersity values as our soils.

We performed semiquantitative X-ray diffraction (XRD) measurements to infer the bulk mineralogy of soils (*Materials and Methods*). This technique has several important limitations: it can only detect crystalline phases, so any amorphous materials are unmeasured, and minerals with similar crystal structure, such as some micas and clays, cannot be easily separated. All samples were composed of three main components of interest: silica, micas such as muscovite, and clays including illite and kaolinite (*SI Appendix*, Fig. S1). We were unable to differentiate some minerals such as muscovite and illite, so we examine the fraction of micas + clays as a proxy for bulk clay content (*SI Appendix*, Text S3). This fraction varied by a factor of two across the samples; given the highly nonlinear dependence of yield stress on clay content (8, 16, 17), we expect a significant effect of cohesion on rheology for these natural soils.

Rheology of Soil Suspensions. We used a parallel-plate rheometer with the following specifications: the top plate diameter of 4 mm, a gap of $h = 1$ mm, sample volume of 5 mL, and a shear rate range of $0.01\ s^{-1} \leq \dot{\gamma} \leq 100\ s^{-1}$. The choice of a small gap size is essential for eliminating two effects that would confound interpretation: sedimentation and grain size segregation, both of which are transient phenomena that violate assumptions of steady and uniform shear within the rheometer. To determine whether the

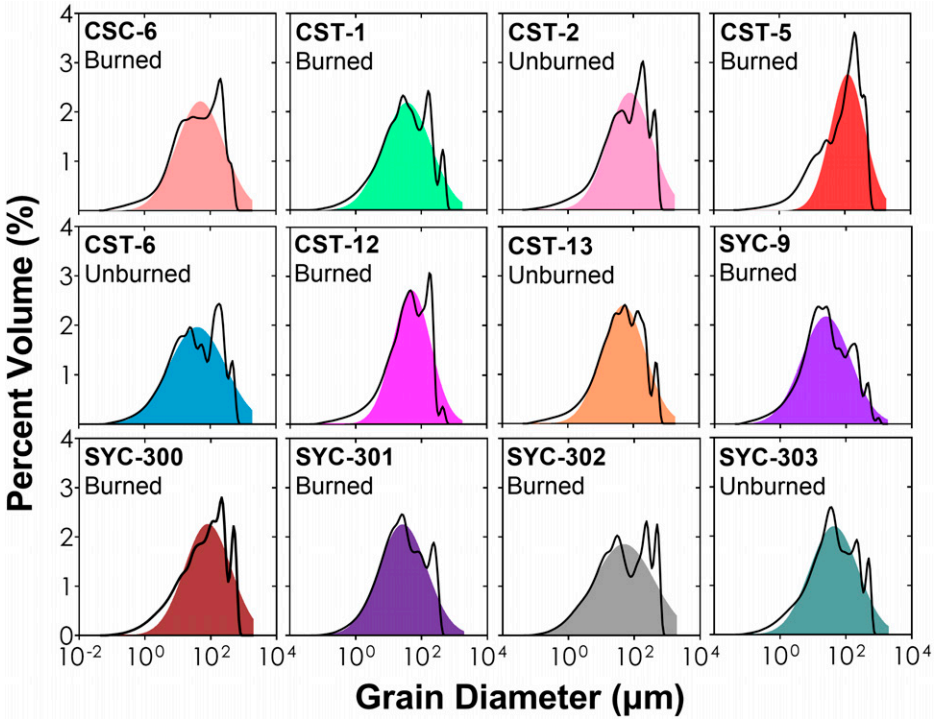

Fig. 2. Grain size distributions for all debris flow source material samples; labels for each correspond to sample locations shown in Fig. 1. Samples exhibit the most similarity in their content for grain sizes of silt and smaller (<60 μm). A strong peak in the fine sand range (∼200 μm) is present for all samples. Most materials also display a peak in the coarse sand range (∼500 μm), but this peak shows the greatest difference between samples. Log-normal distributions are shown that were fit in order to estimate the polydispersity for each sample, and color code for each sample is used for all figures.

measurements in the parallel-plate rheometer were representative of the natural debris flow materials, we also conducted separate experiments using a cup-and-vane rheometer on larger samples of unsieved materials (*SI Appendix*, Text S4). The measured flow curves showed similar scaling to the results from the parallel-plate rheometer (*SI Appendix*, Fig. S2). Sedimentation and segregation phenomena observed in the cup-and-vane rheometer, however, frustrated our efforts to isolate the control of material properties on viscosity. Thus, we do not interpret cup-and-vane flow curves.

The particle pressure associated with sedimentation sets a minimum scale for reliable stress estimates as lower stresses may be insufficient to keep grains in suspension; for our materials this corresponds to $\tau \sim 10^{-1}$ Pa (*Materials and Methods*). The rheometer used for this study measured shear stress. Normal stresses were too small to be reliably measured, given the limited sensitivity of the pressure sensor. Furthermore, earlier studies have shown that the normal stresses are negligible for shear thinning suspensions interacting via hard sphere (54) and attractive potentials (55). Thus, we did not focus on the normal stresses for debris suspensions that exhibit yielding and subsequent shear thinning. We are interested in comparing steady-shear behavior, so we adopted a shear protocol designed to minimize transient effects and hysteresis (56): samples were presheared at the highest rate ($\dot{\gamma} = 100$ s^{-1}) to break up aggregates, and then $\dot{\gamma}$ was ramped down in steps to the minimum value and back up. This is a standard preparation protocol for removing inherited particle structure in yield stress materials (57–59). Although sample rheology may differ from natural debris flow conditions, this procedure allows us to directly compare results across different materials by removing sample-specific memory. We averaged shear stress values at each step (*Materials and Methods*) to produce flow curves (τ vs. $\dot{\gamma}$) for each suspension. For a given soil sample, we prepared suspensions at several volume fractions in the range $0.05 \leq \phi \leq 0.50$ by mixing particulates with deionized water. The highest achievable ϕ is limited by instrument errors that occur as material jams. In connecting these rheometer measurements to the formation of debris flows on the hillslopes, one can envision suspensions with increasing ϕ as representing snapshots along the hillslope profile from ridge to valley. In this manner, the rheometer measurements may inform the evolution in flow behavior as water progressively entrained soil downslope.

Flow curves for all samples confirm that as ϕ is raised, shear stress and viscosity increase, and the suspensions develop a yield stress—evident as a near-constant τ at low $\dot{\gamma}$ (Fig. 3). All flow curves can be closely fit with the Herschel–Bulkley model (Eq. **1**) which allows estimation of yield stress (τ_0) and flow index (n). The lower limit for reliable estimates of yield stress is $\tau_o = 0.1$ Pa (*Materials and Methods*), and the highest observed values reach $\tau_o \approx 200$ Pa. Most suspensions with $\phi \geq 0.2$ appear to be shear thinning ($n < 1$); however, values for n vary widely from 0.37 up to 1.45. Based on the discussion above, we suspect this is because the effects of ϕ, cohesion, and friction have not been separated.

To isolate the effects of ϕ on viscosity, we estimate $\eta(\phi)$ as the viscosity in the high-shear limit that is independent of $\dot{\gamma}$. In curves of $\eta(\phi)$ vs. $\dot{\gamma}$, this corresponds to the regime where $\eta(\phi)$ achieves a constant minimum value (Fig. 4, *Inset*), and flow is approximately Newtonian (60). Importantly, this observed Newtonian plateau indicates that all suspensions remained in the viscous regime. The maximum shear rate, $\dot{\gamma} = 10^2$ s^{-1}, results in a Stokes number $St \approx 3$, consistent with observations of a viscous regime (34). For each soil, $\eta(\phi)$ appears to increase rapidly with ϕ beyond a certain value (Fig. 4, *Inset*); however, that value is different for each material. We estimate the jamming fraction for each of our soils by fitting a divergence relation to the viscosity measurements in the Newtonian regime (Fig. 4), where ϕ_m is a free parameter (60). The inferred jamming fractions

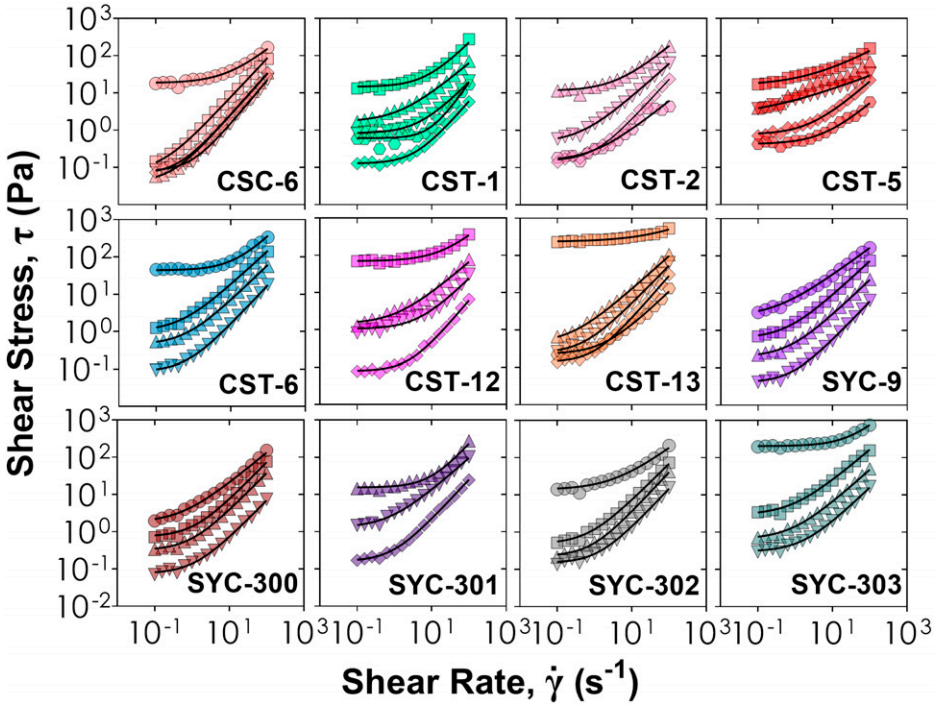

Fig. 3. Shear stress flow curves for various volume fractions (ϕ), for each soil sample analyzed. Only curves for which most measurements satisfy $\tau \geq 0.1$ Pa, the minimum reliable shear stress (*Materials and Methods*), are shown here. Different ϕ values are indicated by their shape (circles, $\phi = 0.50$; squares, $\phi = 0.45$; upward triangles, $\phi = 0.40$; downward triangles, $\phi = 0.35$; diamonds, $\phi = 0.30$; and hexagons, $\phi = 0.20$), while the different samples are color coded as in Fig. 2. For all samples, shear stress increases by multiple orders of magnitude as the volume fraction increases from 0.20 to 0.50. Black lines show Herschel–Bulkley fits from Eq. **1** for each ϕ value.

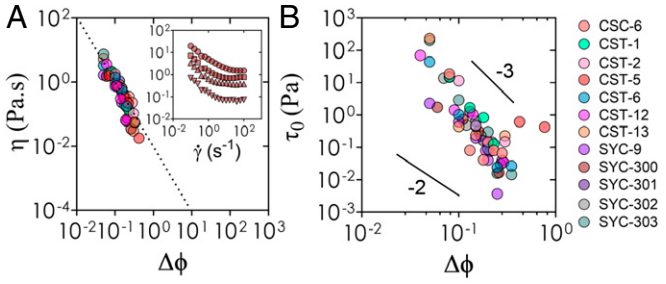

Fig. 4. Rheology depends on the distance from jamming. Scaling of (*A*) viscosity (η) and (*B*) yield stress (τ_0) with the distance from jamming, $\Delta\phi = \phi_m - \phi$. The black dotted line in *A* shows the expected -2 scaling from the rheology of idealized dense suspensions (33). (*Inset*) The viscosity (η)–shear rate ($\dot{\gamma}$) flow curves for an example material (SYC-300) for ϕ values of 0.50 (circles), 0.45 (squares), 0.40 (upward triangles), and 0.35 (downward triangles). Note that η decreases with $\dot{\gamma}$ but approaches a constant value in the high-shear limit. This limiting viscosity $\eta(\phi)$ was used to estimate the jamming fraction for each material, by fitting the equation $\eta(\phi) \propto \eta_f(\phi_m - \phi)^{-2}$ to the data. (*B*) Yield stress decreases rapidly with jamming distance, although scatter indicates another factor is necessary to explain the data. The slopes of -3 and -2 indicate the two power laws in our studies—the former for the yield stress as a function of jamming distance (corresponding to data shown in the figure) and the latter for the viscosity—as function of jamming distance. Note that all yield stress values determined from fits at all volume fractions are shown; however, values less than 0.1 Pa may be unreliable.

vary over $0.47 \leq \phi_m \leq 0.57$ among our materials. However, data for all soil samples collapse onto a single curve of $\eta(\phi)$ vs. $\Delta\phi$ (Fig. 4*A*), indicating that these highly heterogeneous soils behave similarly to idealized suspensions once ϕ_m for each material is accounted for. Considering yield stress, τ_o varies from near zero for low-ϕ suspensions to ~200 Pa for the most dense suspensions considered in this study. We hypothesize from previous work (61–63) that in the low-$\dot{\gamma}$ elastic regime, the yield stress also depends on the distance from jamming, $\tau_o \propto (\Delta\phi)^{-C}$, where C is unknown. Data confirm a strongly nonlinear relation with $C \approx 3$ (Fig. 4*B*) but also exhibit significant scatter, indicating that an additional factor is needed to explain the data. We return to this below.

We now have all the results in hand to test the relevant dimensionless constitutive relation. For all suspensions in which a reliable yield stress could be determined (*Materials and Methods*)—i.e., for all dense suspensions—the confining pressure is assumed to be negligible compared to the yield shear stress (37, 54, 55). Also, all flows remained in the viscous regime, and hence, inertia can be neglected. Accordingly, we nondimensionalize the flow curves (Fig. 3) such that $\tau^* = \tau/\tau_o$ and $\Gamma = \eta(\phi)\dot{\gamma}/\tau_o$, where $\eta(\phi)$ is determined by Eq. **2**. The only undetermined variable is $\mu^c(\phi)$, the contact friction contribution. In principle, this parameter is a complicated function of the static and dynamic friction coefficients, shear rate, and ϕ_m (33). Here we consider $\mu^c(\phi)$ a free parameter, however, and choose its value so that the inflection point in the dimensionless flow curves is centered on $\Gamma = 1$. The result is a collapse of all the flow curves, for different materials and volume fractions, onto a single dimensionless master curve (Fig. 5). The master curve is very well captured by the dimensionless equation

$$\tau^* = 1 + \Gamma. \quad [3]$$

This result indicates that the shear stress over the entire range results from adding two stresses: the yield stress associated with elastic behavior at low shear rates and the viscous stress that emerges at high shear rates. In other words, the simplest rheological model for the data is a (dimensionless) Bingham plastic fluid.

Material Controls on Flow Parameters. Three empirically determined parameters are sufficient to provide a complete first-order description of the flow curves for a given suspension of debris flow materials: jamming fraction ϕ_m, yield stress τ_o, and contact friction $\mu^c(\phi)$. These parameters should be material properties that vary with the composition of each soil sample. The jamming fraction was determined from the high-$\dot{\gamma}$ regime where viscosity is independent of $\dot{\gamma}$ and where we expect the influence of cohesion and aggregation to be negligible (64, 65). The data verify that there is no relation between ϕ_m and sample mineralogy (*SI Appendix*, Fig. S3). Variations in ϕ_m are correlated with sample polydispersity (Fig. 6*A*), a result anticipated from studies of idealized suspensions (52, 66). In addition, ϕ_m generally decreases with increasing $\mu^c(\phi)$ (Fig. 5, *Inset*)—consistent with previous findings that increasing particle friction reduces the jamming fraction (45, 46)—although this effect is much weaker than that of polydispersity. We determined earlier that the first-order control on yield stress is the distance from jamming; hence, τ_o and ϕ_m are related. After controlling for this effect, there is weak evidence of a possible higher-order dependence of τ_o on clay content (Fig. 6). Finally, we find that values for ϕ_m are on average about 5% smaller than ϕ_{max}, the maximum possible packing fraction for each material (Fig. 6*C*). This maximum fraction was achieved by strongly centrifuging each sample (*Materials and Methods*).

Discussion

Previous studies on the rheology of debris flow slurries have reported widely varying degrees of shear thinning and even shear thickening (9, 10, 12–14, 18–22), as determined by values for the flow index n from fitting the Herschel–Bulkley model (Eq. **1**). We saw similar variation among our samples (Fig. 3). We identify two issues that are common in published studies of debris flow rheology: 1) they do not separate the effects of volume fraction and shear rate and do not account for the jamming distance and 2) many use a cup-and-vane geometry, which is susceptible to segregation and sedimentation effects. Here we use the viscosity divergence with volume fraction, in the limit where viscosity is independent of shear rate, to isolate the effect of ϕ and extract the jamming fraction ϕ_m, and we perform experiments in a thin-gap rheometer that facilitates isolation of variables.

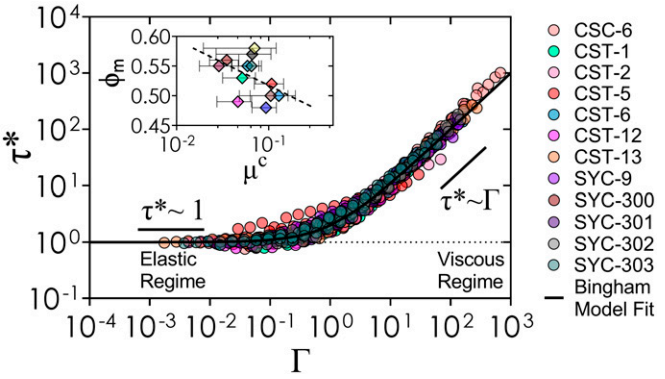

Fig. 5. Nondimensional master flow curve of $\tau^* = \tau/\tau_o$ vs. $\Gamma = \dot{\gamma}/(\tau_o/\eta(\phi))$, showing the collapse of the flow curves for all soil samples at all volume fractions. Two regimes are apparent: a low-Γ regime exhibiting elastic behavior ($\tau = \tau_o$) and a high-Γ viscous regime ($\tau = \eta(\phi)\dot{\gamma}$). The black line is the equation $\tau^* = 1 + \Gamma$, showing that a dimensionless Bingham plastic model (Eq. **3**) provides a good first-order description of the data. (*Inset*) Jamming fraction decreases weakly with the fit-determined contact friction parameter, μ^c. The dashed line is a linear fit to the semilog data with a slope of approximately -0.08 and shows a general trend of decrease in jamming fraction ϕ_m with increasing μ^c.

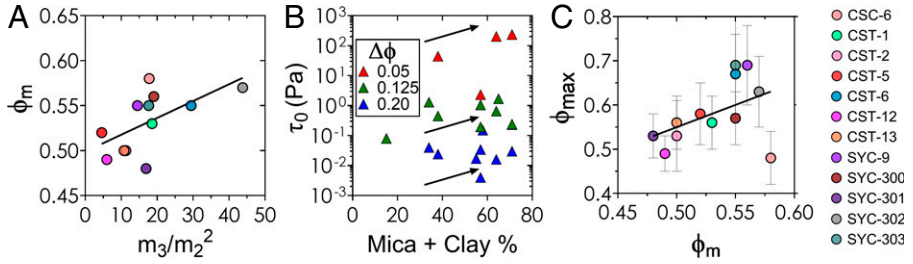

Fig. 6. Material controls on flow parameters. (*A*) Jamming fraction (ϕ_m) linearly increases with the suspension polydispersity (m_3/m_2^2). Dark line indicates a linear fit to data with a slope of 0.0019 ± 0.0008 and *y* intercept of 0.499 ± 0.016. (*B*) Yield stress (τ_0) may increase with clay and mica content (indicated by arrows) once the effect of distance from jamming is removed (indicated in legend); any relation, however, is weak. Note that all yield stress values determined from fits at all volume fractions are shown; however, values less than 0.1 Pa may be unreliable. (*C*) Correlation between the jamming fraction ϕ_m determined from flow measurements and the maximum packing fraction ϕ_{max} estimated from centrifugation. Line is a linear fit of the form $\phi_{max} = a\phi_m + b$ where $a \approx 1.01$ and $b \approx 0.05$. Note that one sample, CSC-6, has the unphysical result that $\phi_m > \phi_{max}$; this sample also showed a nonmonotonic relation between viscosity and ϕ in the high shear rate limit, which suggests that ϕ_m was poorly defined. Right-side legend indicates sample names for *A* and *C*.

We first consider our findings in light of the rheological models introduced at the beginning. The viscous scaling observed in the large Γ limit indicates that inertia is negligible, consistent with our low Stokes numbers. These observations explain why our flow curves collapse when rescaled using the yield stress, in other words, why we see a $\tau^*(\Gamma)$ rheology [rather than a $\mu(I)$ or a $\mu(J)$ rheology]. Results indicate that rheology of our debris flow slurries is well approximated as a Bingham plastic fluid, which suggests a straightforward physical interpretation of our data: flow is determined by the relative strength of the viscous stress compared to the yield stress. The physical picture is that the dense soil slurries examined here are behaving as a hard particle suspension with weak attraction. When Γ is small, cohesion due to fine particles gives rise to a yield stress, manifest as an elastic regime of constant shear stress. For sufficiently large Γ, however, interparticle attraction is negligible, and the samples flow as a linear suspension would. This idea suggests that apparent variations in n, determined from fits to the Herschel–Bulkley relation, may be the result of sampling only a portion of the flow curve. For nearly jammed suspensions with large yield stresses, estimates of n are especially unreliable because stress varies little over the range of shear rates achievable in a rheometer. Although an additional stress associated with plastic dissipation at yield has been proposed to model some suspensions (23), the form of this term is not agreed upon (67, 68), and its inclusion would not improve the fit to our debris flow data.

The most important finding of this study is how the rheology of debris flow source materials is controlled predominantly by the distance from jamming, $\Delta\phi$. Debris flows slurries with similar volume fractions may have very different viscosities and yield stresses, and materials with very different volume fractions may have very similar yield stresses and viscosities. This means that determination of ϕ_m for debris flow source materials is of the utmost importance for modeling the failure and mobility of debris flows in nature. Yet, to the best of our knowledge, no modeling studies have assessed site-specific values of ϕ_m for hillslope soils. Rather, an arbitrary reference value is usually chosen. Our results suggest that the jamming fraction is a meaningful material quantity that is mainly determined by the physical characteristics of particles, i.e., grain size, shape, and roughness. Additionally, values for ϕ_m of our debris flow source materials are on average 5% smaller than the maximum achievable packing fraction ϕ_{max} (Fig. 6*C*), in agreement with previous findings for idealized suspensions (60, 69, 70). This result makes sense because materials at ϕ_{max} must dilate in order to yield and flow. In this regard, ϕ_m is akin to the critical-state volume fraction in soil mechanics (40); it reflects how tightly packed grains are at failure for a given material. Yield stress is strongly related to ϕ_m and is hence controlled by physical characteristics (through friction). From previous work we expect that yield stress should also depend on the chemical composition of soil, in particular the concentration of clay (8, 17), through its influence on cohesion. Our data hint that τ_o is also influenced by clay content for natural debris flow source materials; however, any correlation is not convincing (Fig. 6*B*). The unexpectedly weak relation may be due to our inability to isolate true clay concentration using our methods and/or the highly heterogeneous nature of the soils which include various other materials such as organics that were not characterized. The grain-scale origins of friction and cohesion in highly heterogeneous natural soils deserve deeper scrutiny. From a practical perspective, this means that ϕ_m and τ_o must be determined empirically. Both quantities, however, can be readily obtained from standard rheometry techniques as described here.

It is important to point out the limitations of our findings in terms of their applicability to natural debris flows. Our experiments intentionally eliminated the effects of sedimentation and segregation in order to isolate the influence of particle material properties (polydispersity, friction, and volume fraction) on flow properties. Simulations of natural debris flows must account for such transient and nonuniform effects (28, 40, 71). Moreover, our experiments were conducted under constant volume conditions; this means that the effect of shear-induced Reynolds dilatancy, which is significant for free-surface granular flows like debris flows (40), was suppressed by maintaining a constant gap h in our rheometer. The suspensions exert normal stresses on the walls of the rheometer, which we were unable to probe in our studies. On the other hand, the full suspension rheology model of Boyer et al. (33) includes this effect, which suggests a pathway for extending our results to free-surface conditions. Pore pressure evolution is known to be an important component in the stress balance that drives debris flows (40); a major limitation of steady-shear experiments like ours is that transient variations in pore pressure are neglected. Nevertheless, Eq. **3** may serve as a useful constitutive relation to be included in more sophisticated models (40), while recognizing that rheology alone is insufficient to model natural debris flows (25). At the very least, our findings can help to categorize natural suspensions by their mechanical behaviors. For example, it has been suggested that hyperconcentrated flows are differentiated from more dense debris flows in that the former are Newtonian, while the latter are not (72). Our data indicate that yield stress becomes negligible and flows roughly Newtonian for $\Delta\phi > 0.2$, corresponding to a volume fraction that is less than half of the jamming fraction. For practical purposes, this corresponds to the boundary between dilute and dense suspensions.

This finding may help numerical modelers, who must choose the proper constitutive equation and corresponding solver for routing flows through channels. In terms of extrapolating our rheological findings to field conditions, another limitation is that experiments were conducted under strictly laminar and viscous flow conditions. For debris flows near the jamming transition, the viscosity is sufficiently large that even fully developed flows satisfy laminar conditions. For more dilute suspensions such as hyperconcentrated flows, larger Reynolds numbers (in response to lower volume fractions) result in the influence of turbulence on the effective viscosity. The role of turbulence then must also be considered as hyperconcentrated flows often exhibit behavior more similar to that of Newtonian fluids (73). Similarly, some debris flows in nature likely have large enough grain sizes or shear rates that $St > 10$ and inertia becomes significant (34). Considering a characteristic shear rate $\dot{\gamma} \sim 1\ s^{-1}$, the transition from viscous to inertial regimes would occur for grain sizes on the order of several millimeters. The recent study by Tapia et al. (34) suggests a pathway for combining viscous and inertial stresses in order to develop constitutive relations that span the transition.

Our results, derived from steady-shear experiments, are most directly relevant for modeling and understanding the runout of debris flows. More speculatively, we consider how our results may inform the formation of debris flows by progressive bulking up—the inferred mechanism for the Montecito debris flows (4)—through a thought experiment. Beginning with clear water ($\phi = 0$), viscosity first increases linearly with ϕ as sediment is entrained in the dilute regime (Eq. **2**). The shear stress $\tau = [\rho_p \phi + \rho_w (1 - \phi)] gHS$, where ρ_w is water density, also increases roughly linearly with ϕ. This means that the shear rate $\dot{\gamma} = \tau / \eta(\phi)$ would not change significantly as the flow progressively bulks up downslope. On approach to jamming, however, yield stress and viscosity diverge. The shear rate of the flow, $\dot{\gamma} = [\tau - \tau_o(\phi)]/\eta(\phi)$, would rapidly slow down as $\Delta\phi$ approaches zero. As the shear rate of the suspension slows, the soil entrainment rate would diminish (71). These considerations suggest a self-limiting behavior in the maximum ϕ that can be achieved by progressive bulking up on hillslopes. A previous field study estimated that soil erosion in the 2018 Montecito event created debris flows on the hillslopes that achieved a volume fraction of $\phi = 0.51$ just before entering valley-bottom channels (4). This value sits right in the middle of the range of jamming fractions we determined from rheological measurements of hillslope soils ($0.47 \leq \phi_m \leq 0.57$). This suggests to us that the Montecito debris flows were close to the jamming fraction. An independent estimate confirms this: the yield stress and viscosity of the Montecito debris flows, inferred from downstream observations, can only be reproduced in the laboratory under conditions that are very close to jammed ($\Delta\phi \sim 10^{-2}$; Fig. 4).

We end with an important question that is not answered by our rheological analysis: what was the role of burning in debris flow initiation? There was no systematic difference between burned and unburned soils in terms of grain size, mineralogy, jamming fraction, and rheology. Burning is known to increase soil porosity and decrease effective cohesion, by removing subsurface biomass containing mostly plant roots (74–76). The study by Alessio et al. (4) indicates that fire-induced hydrophobicity of soil significantly enhanced surface runoff by reducing infiltration of rainwater, a common phenomenon observed for postwildfire debris flows (75, 77–79). We suggest that erosion was abetted by the loose state of burned topsoil—i.e., the reduction in volume fraction and effective cohesion—which would make particles more easily entrained by overland flow. In the future, emerging techniques for rapid and sensitive in situ characterization of soil erodibility (80) could be coupled with traditional geotechnical and hydrologic measurements to test and refine this idea.

Materials and Methods

Grain Size. Grain size distributions for each sample were measured using a Beckman-Coulter Particle Size Analyzer LS13-320. Grain size was determined in 114 log-spaced bins over the range 0.04 to 2,000 μm. Each sample was sieved at 0.5 mm, the lower limit of coarse sand; in every case the volume fraction of retained grains was small (< 5% of sample). All distributions contained two or three modes, and in many samples, there appeared to be three distinct grain size populations.

Polydispersity. Polydispersity was measured, following Santos et al.'s (52) previous findings, as m_3/m_2^2, where $m_k \equiv M_k/{M_1}^k$, with M_k being the k^{th} moment of the size distribution. Statistical moments were determined by fitting a lognormal distribution to the grain size data for each sample, using GraphPad Prism version 9.2.0 for Windows (GraphPad Software, www.graphpad.com). The software output includes what we refer to as the amplification factor A, SD σ, and the mean μ. The individual moments for the size distributions are estimated as:

$$M_1 = (1/A)e^{(\mu + 1/2\sigma^2)}, \quad [4]$$

$$M_2 = (1/A)e^{(2(\mu+\sigma^2))}, \quad [5]$$

$$M_3 = (1/A)e^{(3\mu + 9/2\sigma^2)}. \quad [6]$$

The regression analysis of the lognormal fits for the debris flow samples is available in *SI Appendix*, section S6.

Mineralogical Analysis. We utilized semiquantitative XRD measurements to infer mineralogical composition of each sample. Four main component percentages were determined for each sample: clay, quartz, mica, and feldspar. Qualitative and semiquantitative information on the main mineral phases present in each sample was obtained using a Panalytical X'Pert X-Ray Diffractometer (XRD) (81, 82). The system utilized cobalt Kα radiation set to 40 kV and 40 mA. Each sample was pulverized in its entirety with an agate mortar and pestle to manually pass through standard sieve number 325 (diameter <44 μm) before being loaded into a 16-mm-radius slide for analysis. The samples were scanned by the XRD for 3 h at room temperature and relative humidity, using the quartz peak as a natural internal standard to calibrate for peak offsets from deviations in ideal Z height. The instrument operated from 5° to 80° 2θ with a step size of 0.017° 2θ over 4,412 steps. Mineral phases were identified using the Panalytical software program HighScore (82). Mathematical fits were used to determine the phases present along with the relative abundancies in each sample. HighScore's semiquantitative reference intensity ratio technique was used to determine the weight percentage of each mineral phase (83). Due to the chemical similarities between illite clay and mica minerals, these materials could not be differentiated and were lumped together in our analysis. See *SI Appendix*, section S3 for further information.

Rheometry. Rheological measurements were performed in a Bohlin Gemini model parallel plate rheometer, which provides a direct and sensitive measurement of viscosity with no prior calibration (84). All samples were prepared as slurries, a mixture of deionized water and sediment, and tested at $0.05 \leq \phi \leq 0.50$. The samples (5 mL) were inserted between two plates separated by a gap of 1 mm. While shear stresses as low as 10^{-2} Pa were recorded, stress estimates become unreliable at low magnitudes. A minimum reasonable value for stress can be estimated from the particle pressure associated with sedimentation, $\tau_{min} \sim \Delta\rho g a \approx 0.1$ Pa, where $\Delta\rho \approx 1{,}600$ kg/m^3 is the density difference between particles and water and $a = d/2$ is the average particle radius (≈40 μm). Below this stress, particle sedimentation may be expected, which would violate the assumption of uniform mixing within the sample volume. For our sample materials, this lower-stress condition corresponds generally to suspensions with $\phi < 0.20$; accordingly, flow curves for these suspensions are not presented.

A standard protocol was established to ensure reproducibility and to probe hysteresis effects (56). After preshearing, each sample was sheared from a high shear rate, $\dot{\gamma}_{max} \approx 100\ s^{-1}$, to a low shear rate $\dot{\gamma}_{min} \approx 0.01\ s^{-1}$, in 14 equal

steps with a hold time of 20 s at each $\dot{\gamma}$. The downward shear sweep ensured sample homogenization, memory removal, and aggregate breakup. In the next step, samples were sheared from $\dot{\gamma}_{min}$ to $\dot{\gamma}_{max}$ with the same equilibration time (t = 20 s) at each $\dot{\gamma}$. The protocol of down and up shear sweep was performed twice for each sample. The corresponding τ values of the samples were recorded for each $\dot{\gamma}$ and averaged to produce a representative value for each $\dot{\gamma}$ point in a cycle. Given the presence of cohesive/attractive forces, there is a history dependence to the rheology due to the formation and breakup of particle microstructures. At high $\dot{\gamma}$, shear forces overcome the cohesive/attractive forces, but as $\dot{\gamma}$ decreases we expect the aggregates to reform. The ramp cycles allowed us to average out the contribution of the hysteresis to the suspension stress and overall viscosity. Here we consider only the averaged data at each $\dot{\gamma}$ and ignore the hysteresis and time-dependent effects which were found to be of second order.

Herschel–Bulkley Modeling. Data from rheometry measurements were modeled to determine the fit parameters, τ_o and n, for the Herschel–Bulkley model. Model fits were conducted through log-based transformation to calculate nonlinear regressions of each dataset with τ_o, n, and k all left as free parameters. Values of n ranged from 0.37 to 1.45. Values of τ_o ranged over approximately five orders of magnitude, from 10^{-2} Pa to greater than 10^{2} Pa. Values of τ_o less than 10^{-1} Pa were extrapolated from fits of some suspensions but should be interpreted with caution given the estimated τ_{min} for our experiments.

Maximum Packing. Suspensions of soil samples were prepared by adding a known mass of hillslope material (m_p) to a known mass of deionized water ($m_{w,i}$) (subscript i denoting the initial state) and mixing for 30 min. The maximum packing volume fraction for each soil suspension, ϕ_{max}, was obtained by centrifuging the suspension at 2,100 rpm for 20 min. The stresses generated were on the order of 10^3 times the acceleration due to gravity g, which breaks the cohesive/attractive bonds between the particles and forces particles to settle to the bottom of the centrifuge tube forming maximum packed structures. By estimating the difference between the initial amount of water added to prepare the suspension ($m_{w,i}$) and the amount of supernatant water that was discarded after centrifugation ($m_{w,f}$), we estimated the respective ϕ_{max} values for each soil sample using the equation

$$\phi_{max} = \frac{(m_p/\rho_p)}{(m_p/\rho_p) + ((m_{w,i} - m_{w,f})/\rho_w)}. \quad [7]$$

Here ρ_p and ρ_w are the densities of clay particles ($\approx$ 2,600 kg/m^3) and deionized water (1,000 kg/m^3), respectively.

Data, Materials, and Software Availability. All data used within this report are available via Figshare (https://doi.org/10.6084/m9.figshare.20523954.v1) (85). The data file includes the raw rheology, grain size, chemical/mineralogical, and field data in XLSX format used to produce the figures in this report. An additional Python code file of a Hershel–Bulkley fit is provided as a ZIP file.

ACKNOWLEDGMENTS. This project originated at the Physics of Dense Suspensions program at the Kavli Institute for Theoretical Physics, supported by the NSF (NSF PHY-1748958). We are grateful to all participants of that workshop, especially the organizers: Bulbul Chakraborty, Emanuela Del Gado, and Jeff Morris. We acknowledge the funding provided by the Army Research Office (ARO; Grant W911NF2010113) and NSF Materials Research Science and Engineering Center (NSF-DMR-1720530) to D.J. and P.A., Petroleum Research Fund (ACS-PRF Grant 61536-ND8) and NSF National Robotics Initiative (NSF-NRI-INT Award 1734355) to D.J., ARO (Grant W911NF-18-1-0379) to E.M., and the John MacFarlane Foundation to T.D. We also acknowledge Siobhan Whadcoat, Andrew Gunn, Nakul Deshpande, and Bryan Maldonado for helpful discussions. We are grateful to the two referees for outstanding technical and conceptual guidance that helped to reframe the paper.

Author affiliations: [a]Earth and Planetary Sciences, Washington University in St. Louis, St. Louis, MO 63105; [b]Earth and Environmental Science, University of Pennsylvania, Philadelphia, PA 19104; [c]Mechanical Engineering, University of California, Santa Barbara, CA 93106; [d]Ramboll US Consulting Inc., Princeton, NJ 08540; [e]Bren School of Environmental Science and Management, University of California, Santa Barbara, CA 93117; and [f]Mechanical Engineering and Applied Mechanics, University of Pennsylvania, Philadelphia, PA 19104

1. N. R. Regmi, J. R. Giardino, E. V. McDonald, J. D. Vitek, "A review of mass movement processes and risk in the critical zone of Earth" in *Developments in Earth Surface Processes*, J. R. Giardino, C. Houser, Eds. (Elsevier, 2015), pp. 319–362.
2. P. Shen, L. Zhang, H. Chen, R. Fan, EDDA 2.0: Integrated simulation of debris flow initiation and dynamics considering two initiation mechanisms. *Geosci. Model Dev.* **11**, 2841–2856 (2018).
3. S. H. Cannon, E. R. Bigio, E. Mine, A process for fire-related debris flow initiation, Cerro Grande Fire, New Mexico. *Hydrol. Processes* **15**, 3011–3023 (2001).
4. P. Alessio, T. Dunne, K. Morell, Post-wildfire generation of debris-flow slurry by rill erosion on colluvial hillslopes. *J. Geophys. Res.* **126**, e2021JF006108 (2021).
5. J. Kean *et al.*, Inundation, flow dynamics, and damage in the 9 January 2018 Montecito Debris-Flow Event, California, USA: Opportunities and challenges for post-wildfire risk assessment. *Geosphere* **15**, 1140–1163 (2019).
6. T. Takahashi, Debris flow. *Annu. Rev. Fluid Mech.* **13**, 57–77 (1981).
7. X. Huang, M. H. García, A Herschel–Bulkley model for mud flow down a slope. *J. Fluid Mech.* **374**, 305–333 (1998).
8. C. Ancey, Plasticity and geophysical flows: A review. *J. Non-Newt. Fluid Mech.* **142**, 4–35 (2007).
9. P. Coussot, *Mudflow Rheology and Dynamics* (A. A. Balkema, Rotterdam, 1997).
10. J. J. Major, T. C. Pierson, Debris flow rheology: Experimental analysis of fine-grained slurries. *Water Resour. Res.* **28**, 841–857 (1992).
11. P. Coussot, J. M. Piau, On the behavior of fine mud suspensions. *Rheol. Acta* **33**, 175–184 (1994).
12. L. Schippa, *The Effects of Sediment Size and Concentration on the Rheological Behavior of Debris Flows in Granularity in Materials Science* (InTech, 2018).
13. L. Schippa, Modeling the effect of sediment concentration on the flow-like behavior of natural debris flow. *Int. J. Sediment Res.* **35**, 315–327 (2020).
14. R. Sosio, G. B. Crosta, Rheology of concentrated granular suspensions and possible implications for debris flow modeling. *Water Resour. Res.* **45**, W03412 (2009).
15. S. W. Jeong, Grain size dependent rheology on the mobility of debris flows. *Geosci. J.* **14**, 359–369 (2010).
16. B. Yu, Y. Ma, X. Qi, Experimental study on the influence of clay minerals on the yield stress of debris flows. *J. Hydraul. Eng.* **139**, 364–373 (2013).
17. P. Coussot, Structural similarity and transition from Newtonian to Non-Newtonian behavior for clay-water suspensions. *Phys. Rev. Lett.* **74**, 3971–3974 (1995).
18. J. D. Parsons, K. X. Whipple, A. Simoni, Experimental study of the grain-flow, fluid-mud transition in debris flows. *J. Geol.* **109**, 427–447 (2001).
19. C. J. Phillips, T. R. Davies, Determining rheological parameters of debris flow material. *Geomorphology* **4**, 101–110 (1991).
20. P. Coussot, M. Meunier, Recognition, classification and mechanical description of debris flows. *Earth Sci. Rev.* **40**, 209–227 (1996).
21. A. M. Pellegrino, L. Schippa, A laboratory experience on the effect of grains concentration and coarse sediment on the rheology of natural debris-flows. *Environ. Earth Sci.* **77**, 749 (2018).
22. C. Xia, H. Tian, A quasi-single-phase model for debris flows incorporating non-Newtonian fluid behavior. *Water* **14**, 1369 (2022).
23. M. Caggioni, V. Trappe, P. T. Spicer, Variations of the Herschel–Bulkley exponent reflecting contributions of the viscous continuous phase to the shear rate-dependent stress of soft glassy materials. *J. Rheol.* **64**, 413–422 (2020).
24. R. M. Iverson, The physics of debris flows. *Rev. Geophys.* **35**, 245–296 (1997).
25. R. M. Iverson, "The debris-flow rheology myth." in *International Conference on Debris-Flow Hazards Mitigation* (Ed. 3), D. Rickenmann, C. L. Chen, Eds. (Millpress, 2003), pp. 303–314.
26. R. M. Iverson, Regulation of landslide motion by dilatancy and pore pressure feedback. *J. Geophys. Res.* **110**, F02015 (2005).
27. D. L. George, R. M. Iverson, A depth-averaged debris-flow model that includes the effects of evolving dilatancy. II. Numerical predictions and experimental tests. *Proc. R. Soc., Math. Phys. Eng. Sci.* **470**, 20130820 (2014).
28. K. R. Barnhart *et al.*, Multi-model comparison of computed debris flow runout for the 9 January 2018 Montecito, California post-wildfire event. *J. Geophys. Res.* **126**, e2021JF006245 (2021).
29. R. A. Bagnold, Experiments on a gravity-free dispersion of large solid spheres in a Newtonian fluid under shear. *Proc. R. Soc. Lond. A Math. Phys. Sci.* **225**, 49–63 (1954).
30. GDR MiDi, On dense granular flows. *Eur. Phys. J. E* **14**, 341–365 (2004).
31. P. Jop, Y. Forterre, O. Pouliquen, A constitutive law for dense granular flows. *Nature* **441**, 727–730 (2006).
32. Y. Forterre, O. Pouliquen, Flows of dense granular media. *Annu. Rev. Fluid Mech.* **40**, 1–24 (2008).
33. F. Boyer, É. Guazzelli, O. Pouliquen, Unifying suspension and granular rheology. *Phys. Rev. Lett.* **107**, 188301 (2011).
34. F. Tapia, M. Ichihara, O. Pouliquen, É. Guazzelli, Viscous to inertial transition in dense granular suspension. *Phys. Rev. Lett.* **129**, 078001 (2022).
35. É. Guazzelli, O. Pouliquen, Rheology of dense granular suspensions. *J. Fluid Mech.* **852**, P1 (2018).
36. M. Houssais, C. P. Ortiz, D. J. Durian, D. J. Jerolmack, Rheology of sediment transported by a laminar flow. *Phys. Rev. E* **94**, 062609 (2016).
37. T. T. Vo, S. Nezamabadi, P. Mutabaruka, J. Y. Delenne, F. Radjai, Additive rheology of complex granular flows. *Nat. Commun.* **11**, 1476 (2020).
38. D. Bonn, M. M. Denn, L. Berthier, T. Divoux, S. Manneville, Yield stress materials in soft condensed matter. *Rev. Mod. Phys.* **89**, 035005 (2017).
39. A. J. Liu, S. R. Nagel, The jamming transition and the marginally jammed solid. *Annu. Rev. Condens. Matter Phys.* **1**, 347–369 (2010).
40. R. M. Iverson, D. L. George, A depth-averaged debris-flow model that includes the effects of evolving dilatancy. I. Physical basis. *Proc. R. Soc. Math. Phys. Eng. Sci.* **470**, 20130819 (2014).
41. H. Eilers, Die viskosität von emulsionen hochviskoser stoffe als funktion der konzentration. *Kolloid Z.* **97**, 313–321 (1941).
42. J. F. Morris, F. Boulay, Curvilinear flows of noncolloidal suspensions: The role of normal stresses. *J. Rheol.* **43**, 1213–1237 (1999).

43. K. Kamrin, Non-locality in granular flow: Phenomenology and modeling approaches. *Front. Phys.* **7**, 116 (2019).
44. S. Kim, K. Kamrin, Power-law scaling in granular rheology across flow geometries. *Phys. Rev. Lett.* **125**, 088002 (2020).
45. F. Tapia, O. Pouliquen, É. Guazzelli, Influence of surface roughness on the rheology of immersed and dry frictional spheres. *Phys. Rev. Fluids* **4**, 104302 (2019).
46. M. A. Dafalla, Effects of clay and moisture content on direct shear tests for clay-sand mixtures. *Adv. Mater. Sci. Eng.* **2013**, 1–8 (2013).
47. M. Hermes, M. Dijkstra, Jamming of polydisperse hard spheres: The effect of kinetic arrest. *Europhys. Lett.* **89**, 38005 (2010).
48. K. Morell, P. Alessio, T. Dunne, E. Keller, Sediment recruitment and redistribution in mountain channel networks by post-wildfire debris flows. *Geophys. Res. Lett.* **48**, e2021GL095549 (2021).
49. A. Remaître, J. P. Malet, O. Maquaire, C. Ancey, J. Locat, Flow behaviour and runout modelling of a complex debris flow in a clay-shale basin. *Earth Surf. Process. Landf.* **30**, 479–488 (2005).
50. C. Besso, T. M. P. de Campos, On the evaluation of yield stress of soils for debris flow analysis. *E3S Web Conf.* **92**, 05002 (2019).
51. T. Bisantino, P. Fischer, F. Gentile, G. T. Liuzzi, "Rheological properties and debris-flow modeling in a southern Italy watershed" in *WIT Transactions on Engineering Sciences*, D. de Wrachien, C. A. Brebbia, Eds. (WIT Press, 2010), pp. 237–248.
52. A. Santos, S. B. Yuste, M. López de Haro, G. Odriozola, V. Ogarko, Simple effective rule to estimate the jamming packing fraction of polydisperse hard spheres. *Phys. Rev. E Stat. Nonlin. Soft Matter Phys.* **89**, 040302 (2014).
53. S. Pednekar, J. Chun, J. F. Morris, Bidisperse and polydisperse suspension rheology at large solid fraction. *J. Rheol.* **62**, 513–526 (2018).
54. C. D. Cwalina, N. J. Wagner, Material properties of the shear-thickened state in concentrated near hard-sphere colloidal dispersions. *J. Rheol.* **58**, 949–967 (2014).
55. N. Park, V. Rathee, D. L. Blair, J. C. Conrad, Contact networks enhance shear thickening in attractive colloid-polymer mixtures. *Phys. Rev. Lett.* **122**, 228003 (2019).
56. A. Puisto, M. Mohtaschemi, M. J. Alava, X. Illa, Dynamic hysteresis in the rheology of complex fluids. *Phys. Rev. E Stat. Nonlin. Soft Matter Phys.* **91**, 042314 (2015).
57. A. Shakeel, A. Kirichek, C. Chassagne, Effect of pre-shearing on the steady and dynamic rheological properties of mud sediments. *Mar. Pet. Geol.* **116**, 104338 (2020).
58. J. Choi, S. A. Rogers, Optimal conditions for pre-shearing thixotropic or aging soft materials. *Rheol. Acta* **59**, 921–934 (2020).
59. J. E. Taylor, I. Van Damme, M. L. Johns, A. F. Routh, D. I. Wilson, Shear rheology of molten crumb chocolate. *J. Food Sci.* **74**, E55–E61 (2009).
60. S. Pradeep, M. Nabizadeh, A. R. Jacob, S. Jamali, L. C. Hsiao, Jamming distance dictates colloidal shear thickening. *Phys. Rev. Lett.* **127**, 158002 (2021).
61. C. Ancey, H. Jorrot, Yield stress for particle suspensions within a clay dispersion. *J. Rheol.* **45**, 297–319 (2001).
62. G. Ovarlez *et al.*, Flows of suspensions of particles in yield stress fluids. *J. Rheol.* **59**, 1449–1486 (2015).
63. X. Chateau, G. Ovarlez, K. L. Trung, Homogenization approach to the behavior of suspensions of noncolloidal particles in yield stress fluids. *J. Rheol.* **52**, 489–506 (2008).
64. M. Macaulay, P. Rognon, Viscosity of cohesive granular flows. *Soft Matter* **17**, 165–173 (2021).
65. J. Ramírez-Muñoz, G. M. de Jesús, A. Soria, A. Alonso, L. Torres, Assessment of the effective viscous dissipation for deagglomeration processes induced by a high shear impeller in a stirred tank. *Adv. Powder Technol.* **27**, 1885–1897 (2016).
66. K. W. Desmond, E. R. Weeks, Influence of particle size distribution on random close packing of spheres. *Phys. Rev. E Stat. Nonlin. Soft Matter Phys.* **90**, 022204 (2014).
67. E. Lerner, G. Düring, M. Wyart, A unified framework for Non-Brownian suspension flows and soft amorphous solids. *Proc. Natl. Acad. Sci. U.S.A.* **109**, 4798–4803 (2012).
68. J. Lin, M. Wyart, Microscopic processes controlling the Herschel-Bulkley exponent. *Phys. Rev. E* **97**, 012603 (2018).
69. E. Blanco *et al.*, Conching chocolate is a prototypical transition from frictionally jammed solid to flowable suspension with maximal solid content. *Proc. Natl. Acad. Sci. U.S.A.* **116**, 10303–10308 (2019).
70. B. M. Guy, M. Hermes, W. C. Poon, Towards a unified description of the rheology of hard-particle suspensions. *Phys. Rev. Lett.* **115**, 088304 (2015).
71. R. M. Iverson, C. Ouyang, Entrainment of bed material by earth-surface mass flows: Review and reformulation of depth-integrated theory. *Rev. Geophys.* **53**, 27–58 (2015).
72. T. C. Pierson, "Hyperconcentrated flow–Transitional process between water flow and debris flow" in *Debris-Flow Hazards and Related Phenomena*, M. Jakob, O. Hungr, Eds. (Springer, 2005), pp. 159–202.
73. N. C. Calhoun, J. J. Clague, Distinguishing between debris flows and hyperconcentrated flows: An example from the eastern Swiss Alps. *Earth Surf. Process. Landf.* **43**, 1280–1294 (2018).
74. M. B. Bodí *et al.*, Wildland fire ash: Production, composition and eco-hydro-geomorphic effects. *Earth Sci. Rev.* **130**, 103–127 (2014).
75. P. R. Robichaud *et al.*, Infiltration and interrill erosion rates after a wildfire in Western Montana, USA. *Catena* **142**, 77–88 (2016).
76. V. N. Balfour, S. W. Woods, The hydrological properties and the effects of hydration on vegetative ash from the Northern Rockies, USA. *Catena* **111**, 9–24 (2013).
77. E. J. Gabet, Post-fire thin debris flows: Sediment transport and numerical modelling. *Earth Surf. Process. Landf.* **28**, 1341–1348 (2003).
78. K. R. Hubbert, P. M. Wohlgemuth, J. L. Beyers, M. G. Narog, R. Gerrard, Post-fire soil water repellency, hydrologic response, and sediment yield compared between grass-converted and chaparral watersheds. *Fire Ecol.* **8**, 143–162 (2012).
79. S. S. Larson-Nash *et al.*, Recovery of small-scale infiltration and erosion after wildfires. *J. Hydrol. Hydromech.* **66**, 261–270 (2018).
80. F. Qian, D. Lee, G. Nikolich, D. Koditschek, D. Jerolmack, Rapid in situ characterization of soil erodibility with a field deployable robot. *J. Geophys. Res.* **124**, 1261–1280 (2019).
81. H. P. Klug, L. E. Alexander, *X-Ray Diffraction Procedures: For Polycrystalline and Amorphous Materials* (Wiley, 1974).
82. L. Poppe, V. Paskevich, J. Hathaway, D. Blackwood, *A laboratory manual for x-ray powder diffraction* (US Geological Survey, 2001).
83. C. R. Hubbard, R. L. Snyder, RIR–Measurement and use in quantitative XRD. *Powder Diffr.* **3**, 74–77 (1988).
84. T. Y. Liu, D. W. Mead, D. S. Soong, M. C. Williams, A parallel-plate rheometer for the measurement of steady-state and transient rheological properties. *Rheol. Acta* **22**, 81–89 (1983).
85. R. Kostynick et al., Data for "Rheology of debris-flow materials is controlled by the distance from jamming." Figshare. https://figshare.com/articles/dataset/Rheology_of_debris-flow_materials_is_controlled_by_the_distance_from_jamming_zip/20523954/1. Deposited 21 August 2022.